Experimental study of enhanced mixing induced by particles in Taylor–Couette flows

Diane Dherbecourt, Sophie Charton, Fabrice Lamadie, Sébastien Cazin, Éric Climent

Experimental study of enhanced mixing induced by particles in Taylor–Couette flows

D. Dherbécourt[a], *S. Charton*[a,*], *F. Lamadie*[a], *S. Cazin*[b], *E. Climent*[b]

[a] *CEA, DEN, DTEC, SGCS, F-30207 Bagnols-sur-Cèze, France*
[b] *Institut de Mécanique des Fluides, Université de Toulouse, CNRS-INPT-UPS, F-31400 Toulouse, France*

A B S T R A C T

Local mixing dynamics was recently investigated experimentally in Taylor–Couette single-phase flow, thanks to simultaneous Particle Image Velocimetry (PIV) and Planar Laser-Induced Fluorescence (PLIF) techniques. The results highlighted the influence of the successive flow bifurcations and the role of azimuthal wave states on the dispersion of dye injected in Taylor–Couette flows.

The present work extends this study to two-phase configurations with spherical solid particles. The respective effect of particle size and concentration on the vortices size and transition thresholds between the various flow regimes has been examined thanks to flow visualizations and PIV measurements. These hydrodynamic features have been complemented with PLIF experiments, that revealed a drastic enhancement of mixing due to the presence of particles regardless of the flow regime, highlighting the existence of significant particle-induced mixing in Taylor–Couette flows.

Keywords:
Taylor–Couette flows
Mixing enhancement
Suspensions
Coupled PIV–PLIF techniques

1. Introduction

Following the fundamental work of Taylor (1923), flow patterns between two concentric cylinders, depicted in Fig. 1, have been extensively studied. In practical applications involving Taylor–Couette flows (bio and chemical reactors, filtration, etc.), the inner cylinder usually rotates while the outer one stays at rest. Annular centrifugal contactors based on such geometry showed their great potential in the nuclear industry where they are particularly suitable for small-scale studies of solvent liquid–liquid extraction processes, as shown by Davis and Weber (1960). This flow is known to exhibit multiplicity of stable regimes, ranging from laminar Couette flow to turbulence through a sequence of successive hydrodynamic instabilities (Fig. 1), as the rotation rate of the inner cylinder is increased (Andereck et al., 1986).

Beyond a critical Reynolds number (Eq. (1)) based on the gap width e, the rotation rate of the rotor Ω and the fluid viscosity ν (for the case of two-phase flow see mixture viscosity correlations in Einstein (1956) for dilute regime and Stickel and Powell (2005) for dense suspensions), pure Couette flow evolves to toroidal vortices called Taylor Vortex Flow (TVF), which regularly ripple at higher Reynolds numbers. This flow state, designated as Wavy Vortex Flow (WVF) is characterized by an axial wavelength λ and an azimuthal wave number m. As the rotation further increases, this wavy flow becomes modulated by additional frequencies and finally turbulence occurs (Turbulent Taylor Vortex Flow, TTVF). As evidenced by Coles (1965), the occurrence of these flow states and the related hydrodynamic properties depend on the acceleration ramp used to access a given Reynolds number.

$$Re_\Omega = \frac{\Omega R_i e}{\nu} \tag{1}$$

Axial diffusion is an important phenomenon in reactor design, as the amount of mixing within the vortices greatly influences the efficiency of separation processes. In Taylor–Couette flows, mixing results from both intra-vortex

* *Corresponding author*. Tel.: +33 466796229.
E-mail address: sophie.charton@cea.fr (S. Charton).
http://dx.doi.org/10.1016/j.cherd.2016.02.025

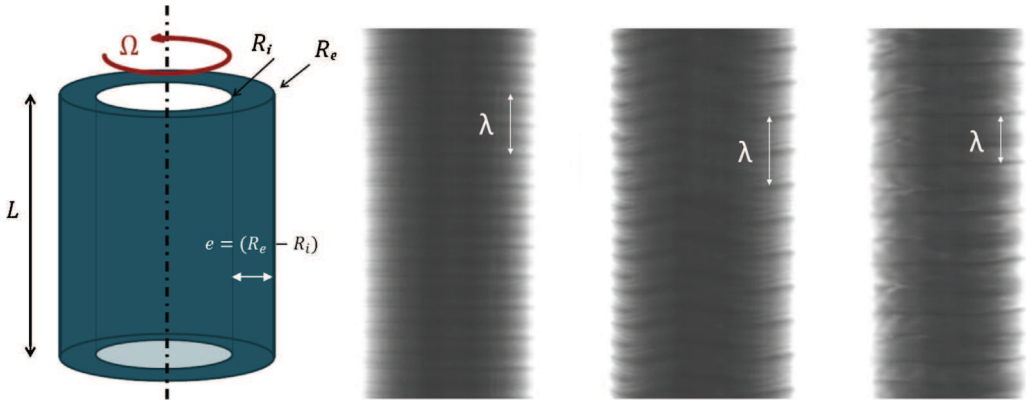

Fig. 1 – Left: Sketch of the Taylor–Couette flow between two concentric cylinders. Right: Flow states visualization, increasing rotation from left to right: TVF, WVF, MWVF, and their corresponding axial wavelengths λ.

mechanisms, related to the rotational flow within each vortex, and inter-vortex mechanisms, controlled by the global flow topology. Our previous study (Nemri et al., 2014) investigated the relation between the dynamics of the single-phase flow and the mixing mechanisms, using simultaneous PIV–PLIF measurements.

In TVF regime, the PLIF measurements revealed a weak intra-vortex mixing, and confirmed the occurrence of dye inter-vortex transport at the vortices outer boundaries. The tracer remains confined in outer layers before being convected towards the separation between vortices, where it can be further transported to the neighboring vortices by diffusion. The weak velocity in the vortices cores carries the tracer very slowly, and mixing in these regions is basically achieved by molecular diffusion across streamlines. Dye transport by both diffusion and convection is well depicted by the 2-zones model proposed by Desmet et al. (1996) to describe mass transfer in TVF.

As the rotation rate increases, the occurrence of wavy motion was shown to enhance mixing noticeably, as a consequence of the local velocity field properties (Akonur and Lueptow, 2003). This was also observed from the more usual dye tracer technique by Ohmura et al. (1997). Indeed, the apparition of traveling waves in WVF breaks the boundaries (closed streamlines) between adjacent vortices and enhances fluid exchange, thus increasing inter-vortex mixing. Wavy motion also yields an enhanced transport of the tracer to the vortex core, supplemented by diffusion, thus increasing intra-vortex mixing as well. The resulting global mixing is therefore noticeably more efficient in WVF than in TVF (Nemri et al., 2014). Moreover, many studies confirmed that mixing properties are very sensitive to the azimuthal wave state (λ, m) in wavy flow, as shown by axial dispersion coefficients determined by DNS and dye tracer experiments by Rudman (1998) and Nemri et al. (2013, 2015).

Regarding liquid–solid flow configurations and taking into account the sensitivity of mixing to hydrodynamics, the influence of the particles on the flow properties is studied. Particle-induced mixing is indeed an important research topic, although very few studies are related to Taylor–Couette flows. Experimental evidence of particle induced mixing was reported by Ajuha (1975) while studying heat transfer in sheared polystyrene suspensions. More recently, Metzger et al. (2013) investigated the effect of shear-induced particle agitation on heat transfer across suspensions, through experiments and numerical simulations in a Couette cell. They highlighted a significant enhancement (>200%) of the suspension transport properties with particles, but concluded that the driving mechanism for this enhanced transport is the translational particle diffusivity. Investigating the influence of particle size, d, particle volume fraction ϕ and applied shear γ, the effective thermal diffusivity α was found to be proportional to the Peclet number $Pe = \gamma d/\alpha$ for $Pe \leq 100$, exhibiting a linear increase of the effective thermal transport properties with the particle concentration for $\phi \leq 40\,\%$. Besides these numerous experimental works, self-diffusion of particles has also been studied theoretically and numerically, as in Abbas et al. (2009) who considered inertial particles in a pure shear flow.

Few studies are dedicated to two-phase Taylor–Couette flows. Most of them are dedicated to bubbly flows, as in the work of Djeridi et al. (2004). Although mixing characterization was not their objectives, the authors investigated the bubbles trajectories and their effects on the flow structure. Modification of the transition thresholds and of the vortices wavelength was highlighted, as well.

This study is part of a more general research program aiming at demonstrating the relevance of Taylor–Couette devices for solvent extraction. One of the most important features of Taylor–Couette flows regarding liquid–liquid extraction is their very low axial mixing, enabling high separation efficiency to be achieved (Lanoë, 2002). In this paper, mixing is investigated in a liquid–solid configuration. Density-matched spherical polymethylmethacrylate (PMMA) particles are used, thus preventing coalescence and breakage events occurring in liquid–liquid dispersions, as well as any sedimentation or creaming phenomena. The particle size (800–1500 μm diameter) and concentration (1–8%) are chosen to be representative of typical laboratory-scale two-phase flow operations.

After a description of the experimental setup of coupled PIV/PLIF experiments, the twofold influence of the particles on the mixing is investigated, considering both the variations of hydrodynamic properties and the particles-induced mixing, depending on the volume fraction.

2. Material and experimental techniques

2.1. *Experimental setup*

The geometric parameters of the experimental device are given in Table 1 and a picture of the setup is presented in Fig. 2. The inner cylinder (rotor) is driven by a speed regulator system. Indeed, because of the flow sensitivity to its transient evolution, the acceleration must be carefully controlled.

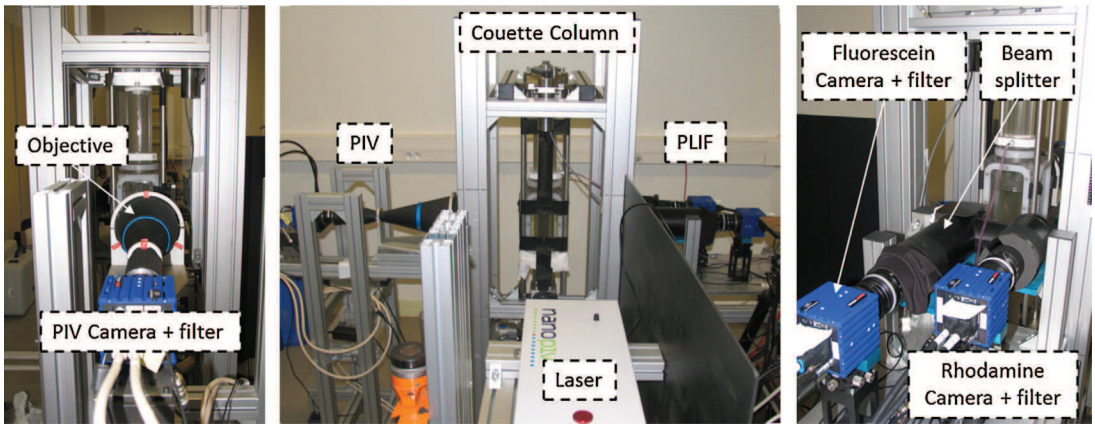

Fig. 2 – Experimental device for the coupled PIV/PLIF measurements.

Table 1 – Geometry of the device.

Stator radius (Re)	35 mm
Rotor radius (Ri)	24 mm
Gap width (e)	11 mm
Radius ratio ($\eta = Re/Ri$)	0.687
Height (H)	640 mm
Aspect ratio ($\Gamma = H/e$)	58
Rotation rate	0.1–100 rad/s

A ramp generator is used to guarantee the reproducibility of the achieved flow regimes.

2.2. *Phase matching*

In order to vary the size and concentration of the dispersed phase, well calibrated solid particles are used. Moreover, to maintain a constant concentration in the visualization test section, the particles are matched in density with the liquid phase to avoid sedimentation or creaming. Additionally, a precise refractive index matching between both phases is required for enable optical measurements such as PIV and PLIF.

PMMA particles of different sizes (800 μm, 1500 μm and 3000 μm diameter) and concentration (ranging from 1% to 16%) are used as the dispersed phase, while the continuous phase is composed of a mixture of dimethylsulfoxide (DMSO), potassium thiocyanate (KSCN) and water. To meet the matching conditions, the relative fraction of each solution compound is adjusted depending on the particle size, as summarized in Table 2.

The corresponding particles characteristics, Eq. (2), calculated in the operating conditions investigated are given in Table 3.

$$St = \frac{1}{9}Re_p = \frac{1}{9}\frac{\gamma d^2}{\nu} = \frac{1}{9}Re\left(\frac{d}{e}\right)^2 \quad (2)$$

Table 3 – Dimensionless numbers characterizing particles under the operating conditions we investigated.

d_p	Flow type	St	Re_p
800 μm	TVF ($Re = 90$)	0.05	0.47
	WVF ($Re = 600$)	0.35	3.19
1 mm	TVF ($Re = 90$)	0.08	0.68
	WVF ($Re = 600$)	0.52	4.67
1.5 mm	TVF ($Re = 90$)	0.18	1.64
	WVF ($Re = 600$)	1.25	11.22

where the shear-rate γ is calculated based on the velocity gradient between the two cylinders:

$$= \frac{\Omega R_i}{e} \quad (3)$$

2.3. *Hydrodynamic properties: direct visualizations and PIV*

Preliminary experiments of flow visualizations are used to study the effect of the particles on the flow regimes. The continuous phase is seeded with small (10 μm) Kalliroscope flakes, consisting in light-reflecting slabs which align themselves along streamlines. They reveal the flow structure and highlight the axial wavelength λ. For the PIV experiments, a double pulsed Nd:YaG laser emitting at 532 nm is used as the light source. The aqueous phase is seeded with hollow glass particles (10 μm diameter) whose density is close to the liquid (1.2 g cm^{-3}). PIV raw images are recorded using a sCMOS camera associated with a bi-telecentric objective of 181 mm working distance, allowing a visualization field of 11 mm × 44 mm, and a pass band filter (532 nm) to remove light coming from the fluorescent tracer. Post-processing of the data yields the relevant velocity field information to characterize the flow state, the position of vortex boundaries and the flow velocity field properties in the gap.

Table 2 – Phase matching (at 23 °C). The volume fraction and mass fraction are equal because of the density matching. The particle mass fraction varies from 1% to 8%.

Solid/liquid phase systems	ρ (g/cm^3)	n	μ (mPa s)
800 μm PMMA particles	1.185	1.4953	–
DMSO 79.81% + KSCN 17.26% + 2.93% water		1.4953	9.513
1 mm PMMA particles	1.185	1.4934	–
DMSO 76.75% + KSCN 18.59% + 4.66% water		1.4935	10.143
1.5 mm PMMA particles	1.185	1.4929	–
DMSO 77.17% + KSCN 17.98% + 4.85% water		1.4926	9.510

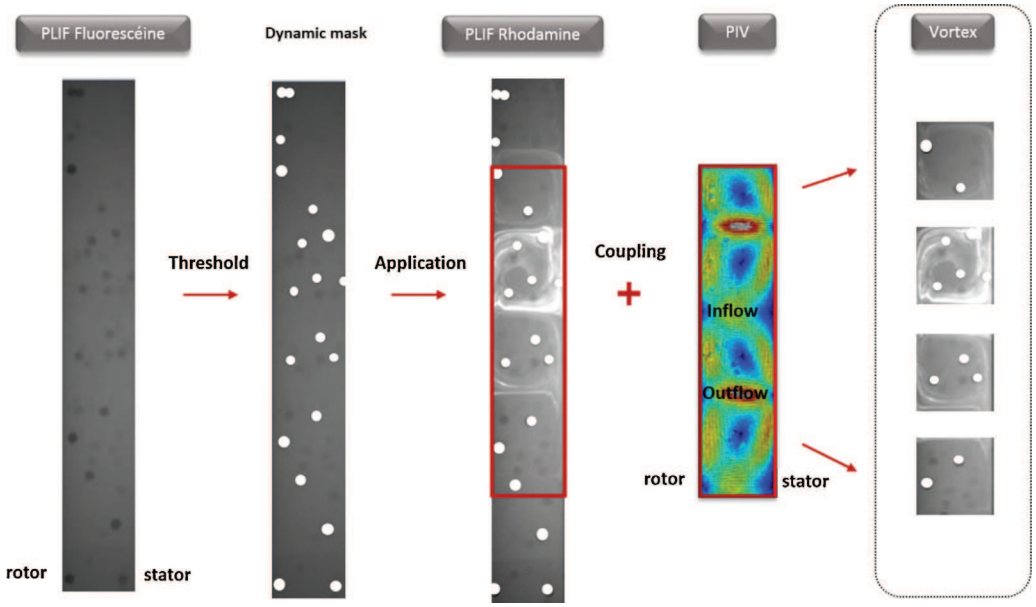

Fig. 3 – Principle of the image processing methodology.

2.4. *Mixing: synchronized PIV–PLIF experiments*

To measure the concentration across the region of investigation, PLIF raw images are generated by a laser plane sheet with the same Nd:YaG laser. Unlike our previous single-phase flow study by Nemri et al. (2014), this PLIF methodology is not sufficient to ensure accurate concentration measurements. Indeed, the presence of particles obstruct locally the concentration measurement, creating holes in the visualization field. Due to the high intensity gradients that appear while injecting the fluorescent dye, a simple threshold technique is not sufficient to detect the particles location.

A new setup based on 2-way PLIF measurements, coupled with PIV, was then proposed for the two-phase experiments. Two fluorescent dyes are simultaneously monitored (Bouche et al., 2013). The first one, Rhodamine WT, is the real PLIF tracer from which the mixing properties of the flow will be investigated. The second one, Fluorescein, is uniformly diluted in the flow and used as a reference. Indeed, measured variations of fluorescein concentration are only due to the presence of particles, making them easier to detect. Thanks to this second PLIF system, dynamic masks of the instantaneous particles surface are created. These masks are achieved by an image processing based on a combination of a threshold and a Watershed segmentation, and are used to correct the PLIF rhodamine raw images, aiming at a better mixing quantification.

Rhodamine WT is injected into the column at a location and a flow rate chosen to not disturb the flow, through an injection capillary located at half the column height, close to the stator wall. Its concentration has been carefully selected to preserve a linear response for the concentration measurement and to keep low absorption effect of the laser sheet by the fluorescent tracer, while keeping a sufficient signal. Note that the injected solution is composed not only of Rhodamine WT at 25 mg/L but also of Fluorescein at 0.5 mg/L, diluted in the DMSO/KSCN/Water mixture, to avoid Fluorescein dilution inside the column. The injection condition is adjusted to the flow state: in the TVF regime, 0.5 mL is injected at 3 mL/min and in WVF regime, 3 mL are injected at 12 mL/min. PLIF images are recorded with two sCMOS cameras, located in front of the PIV camera and observing the same visualization field of 11 mm × 88 mm, thanks to a beam splitter. Specific filters are used to separate Rhodamine fluorescence (625 nm high-pass filter) from fluorescein fluorescence (525 nm low-pass filter). Software and timing box are used to synchronize all devices: laser, PIV and PLIF cameras.

The whole experimental setup is shown in Fig. 2. The room temperature was regulated to 23 °C thanks to an air-conditioner. The fluid temperature was regularly checked in order to detect any increase due to the laser insulation. No evolution has been observed.

Thanks to a previous spatial calibration during the experimental measurements, it is possible to adjust the PIV velocity fields and the PLIF raw images fields. Using the spatial information from PIV, the PLIF images can be separated into distinct vortices, in which the mixing is specifically quantified (Nemri et al., 2015). Fig. 3 depicts how the information from the 3 cameras is used to process the images.

2.5. *Mixing quantification*

The global mixing results from two mechanisms: inter-vortex mixing, observable in the visualization plane, is achieved by the dye migration from one vortex to the adjacent ones. Intra-vortex mixing, representing the dye dispersion inside a given vortex, results from the combination of intra-vortex mixing in the vertical plane (visualization plane), and intra-vortex mixing in the azimuthal direction. Based on the definition of Ottino (1989) and following the work of Dusting and Balabani (2009), a segregation intensity parameter I is introduced to quantify the mixing efficiency, depending on the concentration standard deviation σ_c^2 and the maximum mean concentration σ_0^2 (Eq. (4)). These quantities are computed in different ways to assess both inter- and intra-vortex in each direction (azimuthal and meridional). All measurements of dye concentration are scaled by the injection concentration C_0.

$$I(t) = \frac{\sigma_c^2(t)}{\sigma_0^2(t)} \tag{4}$$

For the inter-vortex mixing, let I_v quantify the mean concentration difference between two adjacent vortices. It is derived from Eqs. (4) and (5) where $\bar{C}_1(t)$ and $\bar{C}_2(t)$ stand for the spatial mean concentration in each of two adjacent vortices, and $\bar{C}(t) = \frac{\bar{C}_1(t)+\bar{C}_2(t)}{2}$ is the mean concentration for these two vortices.

$$\begin{cases} \sigma_c^2(t) = \sum_{i=1}^{2} \left(\bar{C}_i(t) - \bar{C}(t)\right)^2 \\ \sigma_0^2(t) = \bar{C}(t)(1-\bar{C}(t)) \end{cases} \quad (5)$$

Regarding intra-vortex mixing in the vertical plane, the segregation index I_{rz} is defined according to Eqs. (4) and (6). As it represents the tracer dispersion inside a given vortex, $\bar{C}(t)$ stands for the spatial mean concentration within the vortex (corresponding to an area S in the visualization rz plane).

$$\begin{cases} \sigma_c^2(t) = \dfrac{\sum_r \sum_z \left(C_{rz}(t) - \bar{C}(t)\right)^2}{S} \\ \sigma_0^2(t) = \bar{C}(t)(1-\bar{C}(t)) \end{cases} \quad (6)$$

The last segregation index, I_θ, calculated from Eqs. (4) and (7), is representative of the intra-vortex mixing in the azimuthal direction. The mean concentration $\bar{C}(t)$ in Eq. (7) is the time average of the previously defined mean spatial concentration in the rz plane, $\bar{C}_k(t)$, over the K frames recorded during one rotation period of the rotor

$$\begin{cases} \sigma_c^2(t) = \dfrac{\sum_{k=1}^{K} \left(\bar{C}_k(t) - \bar{C}(t)\right)^2}{K} \\ \sigma_0^2(t) = \bar{C}(t)(1-\bar{C}(t)) \end{cases} \quad (7)$$

In all cases, I tends to zero when the perfectly-mixed state is reached. I_v, I_θ and I_{rz} are calculated at each time step to access the temporal evolution of mixing. Three mixing times were additionally defined and used to compare the mixing efficiency of the various contributions: $t_{1/2}$, $t_{1/10}$ and $t_{1/100}$ are respectively the times corresponding to $I_0/2$, $I_0/10$ and $I_0/100$, where I_0 is the value of I at injection time.

In addition, the initial rate of decay R_d of the $I(t)$ evolution is also defined by Eq. (8). R_d is the absolute value of the initial slope of the curves in graphs where I and t are scaled respectively by I_0 and the shear rate γ calculted by Eq. (3). All these parameters are illustrated in Fig. 4.

$$R_d = -\left.\frac{dI}{dt}\right)_{t=0} \cdot \frac{1}{\gamma I_0} \quad (8)$$

In this paper, only I_v and I_{rz} evolutions will be commented. Indeed, mixing in the azimuthal direction (corresponding to I_θ) is very efficient. I_θ tends to zero on very short time scales and overall mixing is simply controlled by I_v and I_{rz} dynamics.

3. Results and discussion

3.1. *Axial wavelength modulation*

The results of the preliminary flow visualizations allowed us to examine the effect of the disperse phase on the flow properties within the annular gap. By probing flows with various wave states (thanks to appropriate start-up procedures), we were able to investigate the effect of the particles on the axial wavelength λ of vortices. Indeed, it is known that λ has a major effect on the mixing efficiency for single phase flows, as shown by Nemri et al. (2014).

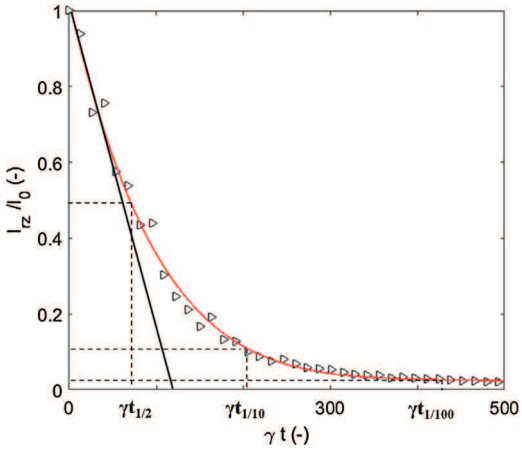

Fig. 4 – Example of the mixing times and initial rate of decay determination, for a I_{rz} curve (white triangles), with the help of a smooth interpolating function (red continuous line). (For interpretation of reference to color in this figure legend, the reader is referred to the web version of this article.)

For a given suspension Reynolds number, the PIV and visualization results evidenced a significant increase of the axial wavelength under two-phase conditions (Table 4 for the TVF regime), regardless of the regime (TVF, SVF or WVF) while increasing the global mixing.

Those preliminary hydrodynamic results, together with the conclusions of the single-phase flow study (Nemri et al., 2014), therefore suggest a significant effect of the dispersed phase on axial mixing through modifications of the flow structure and properties.

To study more specifically the particles influence, the next results about the particle induced mixing are obtained when all the hydrodynamic properties (Re, λ and also m for WVF) are fixed.

3.2. *Particle induced mixing*

The specific influence of the volumetric concentration of particles on each contribution to the global mixing is now studied, thanks to measured $I = f(t)$ evolutions and the corresponding mixing times. Two flow regimes were investigated: the Taylor Vortex Flow and the Wavy Vortex Flow, considering 1 mm diameter particles with particulate volumetric fraction up to 4%. The mass and volume fractions are equal, thanks to density matching between the two phases.

3.3. *Intra-vortex mixing*

PLIF measurements in the vertical plane highlight that mixing is promoted in two-phase flow (Fig. 5), linearly with the

Table 4 – Influence of a dispersed phase (1.5 mm diameter beads) on the axial wavelength λ, in TVF regime for different Reynolds numbers.

Re	Single-phase	Two-phase ($\phi = 4\%$)	Two-phase ($\phi = 8\%$)
88	1.96*e*	2.08*e*	2.26*e*
108	2.06*e*	2.16*e*	2.37*e*
126	1.97*e*	2.32*e*	2.63*e*

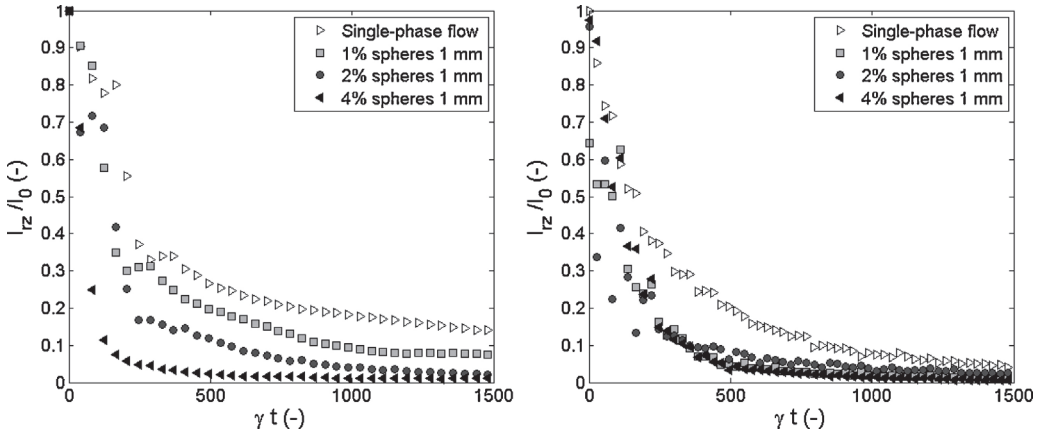

Fig. 5 – Influence of the particle concentration on the inter-vortex mixing I_{rz} in TVF regime (left: $Re = 90$, $\lambda = 2 \cdot 10e$) and WVF regime (right: $Re = 600$, $\lambda = 2.05e$, $m = 3$).

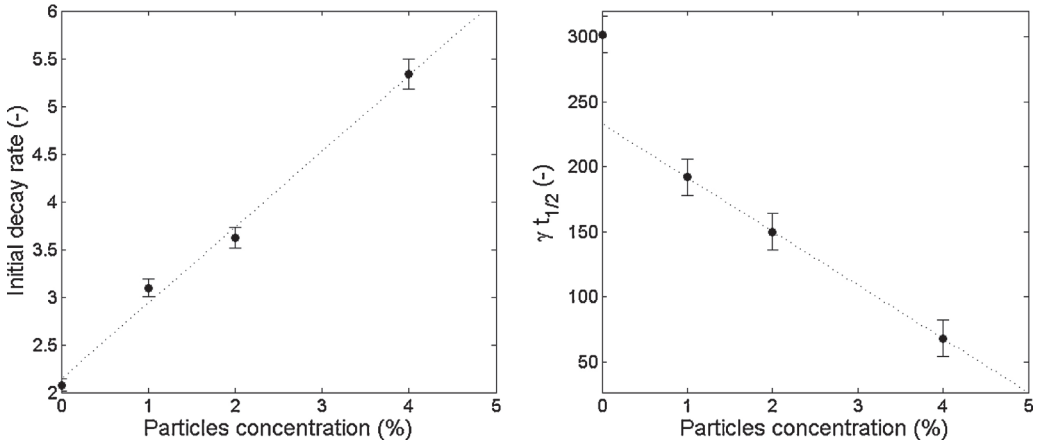

Fig. 6 – Evolution of the initial rate of decay (left) and the mixing time $\gamma t_{1/2}$ (right) depending on the particle concentration (linear fitting for the dotted line) in TVF regime ($Re = 90$, $\lambda = 2.10e$).

particle concentration in TVF (Table 5 and Fig. 6). For WVF, the influence of particles is less pronounced (Fig. 5, right).

3.4. *Inter-vortex mixing*

In TVF, a significant increase of inter-vortex mixing is evidenced for a concentration above 1% in the case of 1 mm diameter particles, highlighting the inter-particle effects. The effect is enhanced when the concentration of particles is increased (Table 6 and Fig. 7). In WVF, a particle-induced mixing is also revealed by the PLIF results and observed to increase with the particle concentration.

3.5. *Discussion*

Two distinct mechanisms have been observed while investigating the effect of a dispersed phase on the mixing efficiency of Taylor–Couette flows.

First, flow visualizations and PIV measurements indicate that the hydrodynamic properties, to which mixing is strongly related, are highly sensitive to the presence of a dispersed phase.

Besides those hydrodynamic effects, PLIF experiments achieved while carefully controlling the flow state (*i.e.* same *Re*, same λ and for WVF same *m*) highlight an intrinsic effect of the particles on the mixing efficiency. The general trend observed is an increase of the tracer mixing in all the three directions (r, z, and θ).

Four kinds of forcing may apply on particles in a viscous suspension, and could be responsible of this mixing enhancement: (i) the drag related to fluid flow and hydrodynamic interactions, (ii) Brownian agitation, (iii) inertial effects and (iv) inter-particle interactions such as collisions. All those contributions produce particle agitation which can lead to

Table 5 – Mixing time $\gamma t_{1/2}$ and initial decay rate for I_{rz} in TVF ($Re = 90$, $\lambda = 2.10e$).

Particle concentration	$\gamma t_{1/2}$	Initial rate of decay
Single-phase flow	302	$2.08 \cdot 10^{-3}$
1%	192	$3.10 \cdot 10^{-3}$
2%	150	$3.62 \cdot 10^{-3}$
4%	68	$5.34 \cdot 10^{-3}$

Table 6 – Mixing time $\gamma t_{1/2}$ and initial decay rate for I_v in TVF ($Re = 90$, $\lambda = 2.25e$) and in WVF ($Re = 600$, $\lambda = 2.05e$, $m = 3$), associated to Fig. 7.

Flow state	Particle concentration	$\gamma t_{1/2}$	Initial rate of decay
TVF	Single-phase flow	672	$0.83 \cdot 10^{-3}$
TVF	1%	535	$1.11 \cdot 10^{-3}$
TVF	4%	452	$1.24 \cdot 10^{-3}$
WVF	Single-phase flow	370	$1.54 \cdot 10^{-3}$
WVF	1%	288	$2.17 \cdot 10^{-3}$
WVF	4%	205	$2.72 \cdot 10^{-3}$

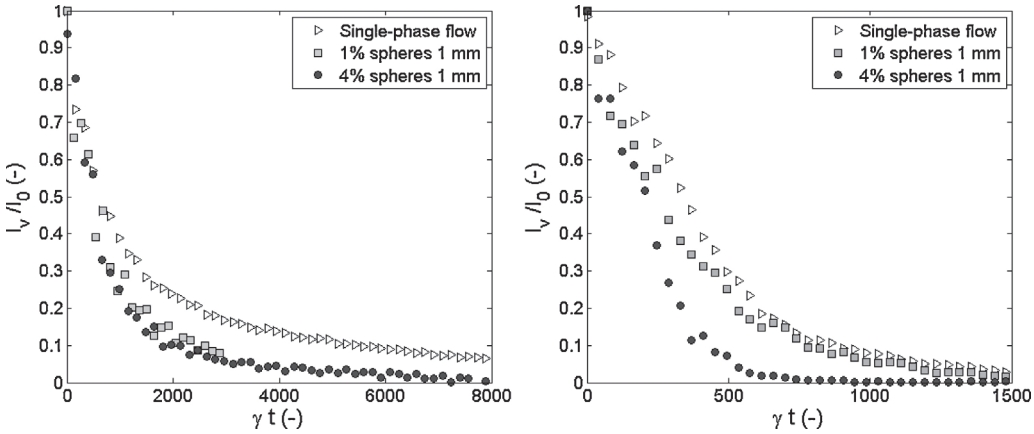

Fig. 7 – Influence of the particle concentration on the inter-vortex mixing I_v in TVF regime (left: $Re = 90$, $\lambda = 2.25e$) and WVF regime (right: $Re = 600$, $\lambda = 2.05e$, $m = 3$).

enhancement of tracer dispersion in a flow under two-phase conditions.

(i) The particles are embedded in a viscous fluid which drags them along the flow. Due to their macroscopic size they may not follow exactly the streamlines (Faxen correction to the drag) and hydrodynamic interactions yield flow perturbations around each particle.

(ii) In our case, Brownian diffusion can be neglected as the particles we considered are large ($d \gg 10\,\mu$m) and non-colloidal (Breedveld, 2000). The Peclet number, $Pe = \gamma e^2/D$, based on Stokes–Einstein diffusion coefficient would be extremely large.

(iii) The estimate of the impact Stokes number, $St = 1/9 \times \gamma d^2/\nu$, i.e. a dimensionless measure of the relative velocities of two particles experiencing a collision in a shear flow, shows that the kinetic particle energy after their collisions, if any, is entirely absorbed by the surrounding fluid (Brändle de Motta et al., 2013; Yang and Hunt, 2006). Hence, particles agitation due to collisions is weak, and the effect of inertia on mixing can be neglected too under our experimental conditions.

(iv) Finally, inter-particle interactions are considered. The latter are composed of gradient diffusion and shear-induced self-diffusion. Gradient diffusion, due to the higher resistance experienced by a particle moving into regions of dense concentration compared to the same particle evolving in dilute suspension, results in a drift of the particles from the regions of high to low particle concentration. Because the spatial particle distribution is close to uniform in our experiments, the mixing behavior can hardly be attributed to the gradient diffusion, proving that the main mechanism of interest in our case is more likely the shear-induced self-diffusion, illustrated in Fig. 8.

Similarly to heat transfer, the tracer dispersion efficiency is expected to grow linearly with the particle concentration for dilute suspensions because of the shear-induced particle agitation (see Fig. 8). This is in good agreement with our results about the intra-vortex mixing in TVF. However the inter-vortex efficiency in TVF does not show a linear evolution as a function of the particle volume fraction, due to two combined mechanisms. On one hand, shear-induced particle agitation occurs. On the other hand, the particles interact with the vortices outer layers, that are surrounding the cores, where poor mixing is observed. Experimentally, the characteristic thickness of those layers is estimated to 850 μm in single-phase flow. When the particles are moving in this zone where the convection is important, they drag dye while breaking the closed streamlines between adjacent vortices (as evidenced in Fig. 9), leading to a non-monotonous enhancement of the inter-vortex mixing with increasing particle size. Small particles do not affect mixing while bigger ones ($d = 1$ mm, $d = 1.5$ mm) are observed to increase mixing efficiency.

The evolution of intra-vortex mixing with particle concentration ϕ in WVF strays from linearity. This could be due to a

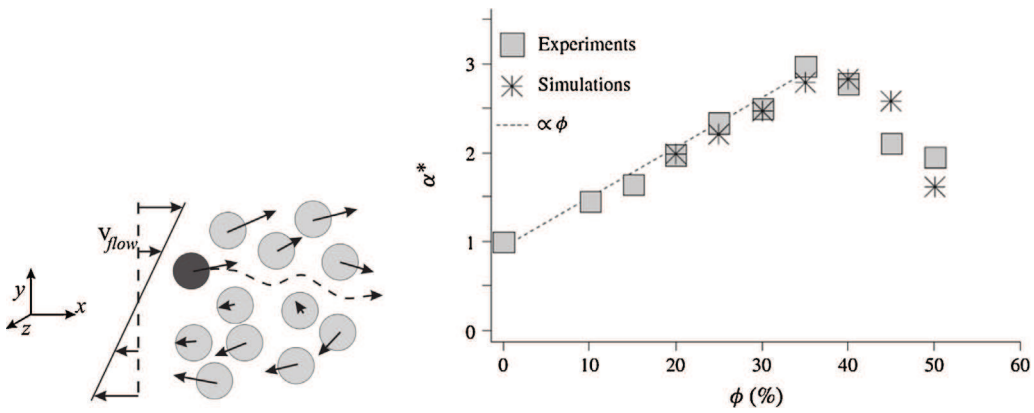

Fig. 8 – Left: Illustration of the shear-induced self-diffusion of particles (from Breedveld, 2000). Right: Effective thermal diffusion coefficient as a function of the volume fraction (from Metzger et al., 2013).

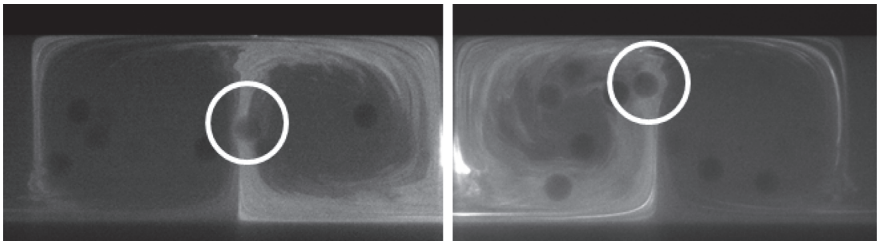

Fig. 9 – Illustration of dye dragged by a particle through closed streamlines between adjacent vortices.

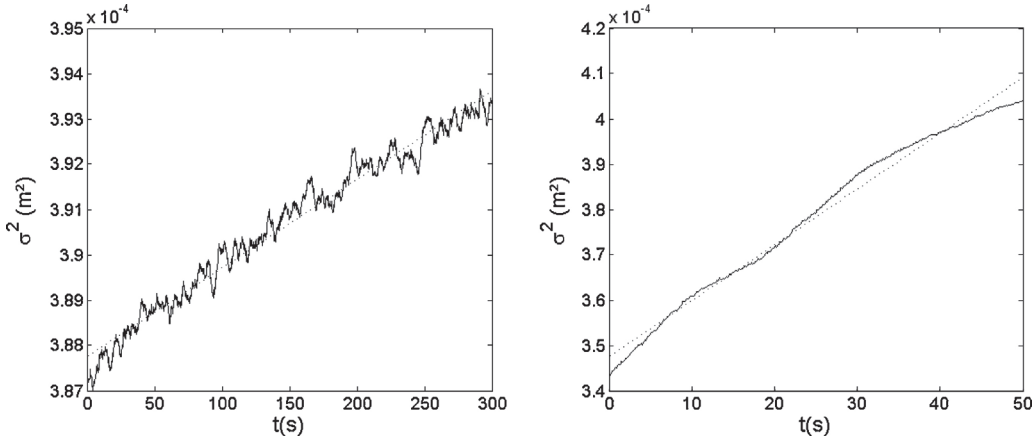

Fig. 10 – Evolution of the variance σ^2 as a function of time, in TVF (left) and in WVF (right).

combination of two physical mechanisms: the shear-induced self-diffusion and the modulation of the vortices structure in presence of particles.

The inter-vortex mixing efficiency exhibits a linear evolution with the dispersed phase concentration in WVF. This result, also observed with other particle sizes, highlights the shear-induced diffusion as the driving mixing mechanism.

3.6. *Effective axial mixing*

As we did for single-phase flow (Nemri et al., 2015), the next step of this work is to establish a relation between the local mixing kinetics and the axial dispersion coefficient, D_{ax}, commonly used in chemical engineering studies. A first attempt can be made from the time-evolution of the rhodamine tracer spreading measured in PLIF experiments. Considering the axial dispersion as a diffusional mechanism, the linear evolution of the variance $\sigma^2(t)$ as a function of time gives an estimation of D_{ax}. Using $\bar{z}(t)$ as the instantaneous mass centroid, m_0 for the total tracer concentration (Eq. (9)) and $C(x, y, t)$ the instantaneous tracer concentration, following Aris (1956), the variance is given by Eq. (10).

$$\begin{cases} \bar{z}(t) = \dfrac{1}{m_0}\displaystyle\int_x\int_y \rho x C(x,y)\mathrm{d}x\,\mathrm{d}y \\ m_0 = \displaystyle\int_x\int_y \rho\, C(x,y)\mathrm{d}x\,\mathrm{d}y \end{cases} \tag{9}$$

$$\sigma^2(t) = \frac{1}{m_0}\int_x\int_y \rho\,(x-\bar{z}(t))^2\, C(x,y,t)\,\mathrm{d}x\,\mathrm{d}y \tag{10}$$

Typical evolution of σ^2 as a function of time is illustrated in Fig. 10, in TVF and in WVF regimes. The effective diffusion coefficient D_{ax} represents the slope of this curves. This method, applied to 6 vortices, presents however important relative error (40%). Indeed, as the visualization area is small, the dye escapes quickly outside and the curves slope evolves with time. The D_{ax} orders of magnitude ($1.2\cdot10^{-4}$ cm^2/s in TVF and $6.2\cdot10^{-3}$cm^2/s in WVF) allows us to clearly distinguish the flow states.

4. Conclusion

Global mixing enhancement in two-phase flow is the result of two combined effects: first, the particles modify the hydrodynamic parameters (stability of regimes and axial wavelength). Additionally, the specific influence of finite-size particles, due to inter-particle interactions, significantly enhances mixing. Possible physical mechanisms have been proposed to explain these experimental evidences.

Our experimental study aimed at quantifying the mixing at local scale. In order to predict the global efficiency of mixing, a relation has to be found to link these small scale observations to a global dispersion coefficient of the flow D_{ax}. In this purpose, three ways are usually proposed. The first one consists in experimental DTS measurements, enabling the calculation of D_{ax} by comparison with existing chemical engineering models. The second one is a numerical approach coupling DNS and Lagrangian tracking, investigating the influence of a dispersed phase on the mixing. These two methods were used by Nemri et al. (2013, 2015). Here, we propose to use an alternative approach based on the global variance of the tracer concentration observed during the PLIF local measurements to quantify axial mixing.

Acknowledgments

The authors thank Hervé Roussel from CEA and Moïse Marchal from IMFT for their technical support. This work was supported by the Nuclear Energy Division of CEA (program DISN/PAREC).

References

Abbas, M., Climent, E., Simonin, O., 2009. Shear-induced self diffusion of inertial particles in viscous flow. Phys. Rev. E 79, 036313.

Ajuha, A., 1975. Augmentation of heat transport in laminar flow of polystyrene suspensions. J. Appl. Phys. 48, 3417–3425.

Akonur, A., Lueptow, R., 2003. Chaotic mixing and transport in wavy Taylor–Couette flow. Physica D 167, 183–196.

Andereck, C., Liu, S., Swinney, H., 1986. Flow regimes in a circular Couette system with independently rotating cylinders. J. Fluid Mech. 164, 155–183.

Aris, R., 1956. On the dispersion of a solute in a fluid flowing through a tube. Proc. R. Soc. 235, 67–77.

Bouche, E., Cazin, S., Roig, V., Risso, F., 2013. Mixing in a Swarm of bubbles rising in a confined cell measured by mean of PLIF with two different dyes. Exp. Fluids 54, 1552.

Brändle de Motta, J., Breugem, W., Gazanion, B., Estivalezes, J., Vincent, S., Climent, E., 2013. Numerical modelling of finite-size particle collisions in a viscous fluid. Phys. Fluids 25, 083302.

Breedveld, V., 2000. Shear-Induced Self-Diffusion in Concentrated Suspensions. University of Twente, Enschede (Ph.D. thesis).

Coles, D., 1965. Transitions in circular Couette flow. J. Fluid Mech. 21, 385–425.

Davis, M., Weber, E., 1960. Liquid–liquid extraction between rotating concentric cylinders. Ind. Eng. Chem. 52, 929–934.

Desmet, G., Verelst, H., Baron, G., 1996. Local and global dispersion effect in Taylor–Couette flow – I. Description and modeling of the dispersion effects. Chem. Eng. J. 51, 1287–1298.

Djeridi, H., Gabillet, C., Billard, J., 2004. Two-phase Couette-Taylor flow: Arrangement of the dispersed phase and effects on the flow structures. Phys. Fluids 16, 128–139.

Dusting, J., Balabani, S., 2009. Mixing in Taylor–Couette reactor in the non wavy flow regime. Chem. Eng. Sci. 64, 3103–3111.

Einstein, A., 1956. Investigations on the Theory of Brownian Movement. Dover Publications, Inc.

Lanoë, J.-Y., 2002. Performances d'une colonne d'extraction liquide-liquide miniature basée sur un écoulement de Taylor–Couette. In: ATALANTE Conference.

Metzger, B., Rahli, O., Yin, X., 2013. Heat transfer across sheared suspensions: role of the shear-induced diffusion. J. Fluid Mech. 724, 527–552.

Nemri, M., Climent, E., Charton, S., Lanoe, J., Ode, D., 2013. Experimental and numerical investigation on mixing and axial dispersion in Taylor–Couette flow patterns. Chem. Eng. Res. Des. 91, 2346–2354.

Nemri, M., Cazin, S., Charton, S., Climent, E., 2014. Experimental investigation of mixing and axial dispersion in Taylor–Couette flow patterns. Exp. Fluids 55, 1769–1785.

Nemri, M., Charton, S., Climent, E., 2015. Mixing and axial dispersion in Taylor–Couette flows: the effect of the flow regime. Chem. Eng. Sci. 139, 109–124.

Ohmura, N., Kataoka, K., Shibata, Y., Makinov, T., 1997. Effective mass diffusion over cell boundaries in a Taylor–Couette flow system. Chem. Eng. Sci. 52, 1757–1765.

Ottino, J., 1989. The kinematics of mixing: stretching, chaos and transport. Cambridge university Press.

Rudman, M., 1998. Mixing and particle dispersion in the wavy vortex regime of Taylor–Couette flow. AIChE J. 44, 1015–1026.

Stickel, J., Powell, R., 2005. Fluid mechanics and rheology of dense suspensions. Annu. Rev. Fluid Mech. 37, 129–149.

Taylor, G., 1923. Stability of a viscous liquid contained between two rotating cylinders. Philos. Trans. R. Soc. London 223, 289–343.

Yang, F., Hunt, M., 2006. Dynamics of particle–particle collisions in a viscous liquid. Physics of Fluids 18, 121506.